IOP Publishing Phys. Med. Biol. 64 (2019) 175022 (15pp) https://doi.org/10.1088/1361-6560/ab2485

Physics in Medicine & Biology

IPEM Institute of Physics and Engineering in Medicine

PAPER

Shapes and distributions of soft tissue scatterers

K J Parker

Department of Electrical and Computer Engineering, University of Rochester, Computer Studies Building 724, Box 270231, Rochester, NY, 14627, United States of America

E-mail: kevin.parker@rochester.edu

RECEIVED
20 December 2018

ACCEPTED FOR PUBLICATION
24 May 2019

PUBLISHED
5 September 2019

Keywords: scattering, backscatter, ultrasound, tissue, medical ultrasound, fractal vasculature, tissue characterization

Abstract

What causes scattering of ultrasound from normal soft tissues such as the liver, thyroid, and prostate? Commonly, the answer is formulated around the properties of spherical scatterers, related to cellular shapes and sizes. However, an alternative view is that the closely packed cells forming the tissue parenchyma create the *reference media*, and the long cylindrical-shaped fluid vessels serve as the *scattering sites*. Under a weak scattering or Born approximation for the extracellular fluid in the vessels, and assuming an isotropic distribution of cylindrical channels across a wide range of diameters, consistent with a fractal branching pattern, some simple predictions can be made about the nature of backscatter as a function of frequency in soft tissues. Specifically, a number of plausible shapes would predict that backscatter increases as a power law of frequency, where the power law is determined by the function governing the number density of the vessels versus diameter. These results are compared with some historical models developed over the last 100 years in scattering theory and point to the need for higher spatial resolution and higher bandwidths to obtain more precise measures of the key parameters in normal tissues, and to better identify the dominant structures responsible for backscatter in everyday clinical imaging.

1. Introduction

It is well established that the electromagnetic and acoustic scattering from an inhomogeneous medium can be related to properties of the spatial correlation function, a statistical measure of the spatial patterns or fluctuations within the material (Debye and Bueche 1949, Morse and Ingard 1987). Under the Born approximation and assumptions of stationarity, the key integral formula relating the ensemble average measures of backscattered intensity to the material spatial correlation function can be interpreted as a Fourier transform operation. In the long history of scattering measurements, several functions appear repeatedly across vastly different experimental domains, particularly autocorrelation functions related to spheres, exponential decays, and power laws. It is natural to think that these could have application to biological soft tissues, which are comprised of cells that have often been modeled as spheres. This paper re-examines the experimental evidence and common theories to gauge the most likely elements of backscatter from soft tissue. A different picture emerges if we consider the closely packed cells to be the reference media, while the long, cylindrical fluid-filled vessels and extracellular spaces are the weak scattering sites.

Before considering tissue fluid channels, however, we review the major models developed over time from scattering experiments. Because of the common integral kernel for the backscatter equation in both electromagnetic and acoustic regimes under the Born approximation, we examine common themes from both domains as they developed over a century of research.

1.1. Classical structures and functions in scattering

A great wealth of scattering studies has been reported in the 100+ years since Lord Rayleigh's foundational work on light and sound (Rayleigh 1897, 1918, 1945). In this overview, we concentrate on formulations from weak scatterers and resulting distributions. More exact formulations typically involve series expansions (Faran 1951,

Born and Wolf 1980) and are beyond the scope of this discussion. Within the weak scattering formulations, we frequently encounter exponential functions, power law functions, and Gaussian functions.

1.1.1. Optics and electromagnetic scattering

Debye and Bueche (1949) formulated the integral transform relation between the ensemble averaged and normalized correlation function of the material properties, and the resulting scattering. They explicitly considered an exponential correlation and demonstrated that it corresponds to a power law in scattered intensity according to the well-known Fourier transform pair relating $\exp[-r]$ to $1/(1+k^2)$. In a later paper, Debye *et al* (1957) derived an equation for random holes in a material that leads to an exponential correlation function.

Chernov (1960) begins his first chapter with experimental evidence from Lieberman showing an exponential correlation function from measurements of temperature fluctuations in the ocean. He explicitly considers an exponential autocorrelation function and a modified form that has a zero first derivative at the origin. In later chapters, Chernov considers Gaussian and modified Gaussian autocorrelation functions.

Ishimaru (1978b), in his third chapter, displays a number of attenuation and scattering spectra from a range of electromagnetic and bioacoustics experiments. Many of these, such as scattering from bubbles in an aqueous medium, have distinct peak-and-valley characteristics, and thus do not naturally fall within the simple exponential correlation function favored by earlier references.

Tatarskii (1961), in his first chapter, explicitly considers exponential, Gaussian, and modified power law correlation functions of inhomogeneities within turbulent media such as the atmosphere.

Sheppard considered the statistics of coherent imaging of random surfaces, and considered profiles with Gaussian random profiles (Sheppard and Connolly 1995) and then with exponential and fractal profiles (Sheppard and Connolly 1995).

Schmitt and Kumar (1996) measured refractive index variations in tissues and found a power law spectrum from mouse liver tissues, at least over a few decades of spatial frequencies. They related this to a von Karman spectrum which was then linked to a correlation function modeled as a modified Bessel function $K_m[\Delta r]$.

1.1.2. Bioacoustics

Morse and Ingard (1987), in their classical derivation of scattering from weak acoustic scatterers, consider Gaussian and modified Gaussian correlation functions.

Waag (Waag *et al* 1982, 1989a, 1989b, Campbell and Waag 1984b) demonstrated power law behaviors from all ensemble-averaged spectra derived from optical and ultrasound scattering experiments performed on normal and diseased tissue, as well as on bio-mimicking materials. He also considered Gaussian and modified Gaussian correlation models.

Chivers (1977) considered both exponential and Gaussian correlation models in his survey of tissue scattering.

Lizzi *et al* (1983) established a framework for analysis of scattered ultrasound from tissues, including a model of very small scattering sites that were Poisson distributed in space, and then later including spherical shapes that have been incorporated into quantitative ultrasound (QU) studies (Mamou and Oelze 2013).

Insana, Hall, and colleagues (1990) considered three correlation functions for random media, related to fluid spheres, spherical shells, and a Gaussian behavior. These were applied to a number of phantoms and tissues (Insana and Brown 1993).

Shung and colleagues demonstrated the scattering of red blood cells which in a dispersed form exhibit classical Rayleigh scattering behavior at the frequencies commonly used in ultrasound scans of adult humans (Shung and Thieme 1993).

There have also been assessments of possible periodic spacing of structures within tissues, and coherent components of scattering; candidates include portal triads within the liver (Fellingham and Sommer 1984, Insana *et al* 1986, Landini and Verrazzani 1990, Varghese and Donohue 1993, Cramblitt and Parker 1999, Machado *et al* 2006, Rosado-Mendez *et al* 2016). This remains an area of research.

1.1.3. Correlation functions from other natural phenomena

It is fascinating to note some parallel mathematical treatments stemming from other research fields. Whittle, in a series of papers, considered the variations in agricultural yield across time and space, and considered power law, exponential, and modified Bessel function $K_1[\Delta r]$ correlation functions to model the sampled data (Whittle 1954, 1962, 1963). Agterberg furthered this work and applied models to samples of geological variables, with some of the analysis centered on exponential correlation functions of space (Agterberg 1970).

Pedersen (1997) considered smallangle x-ray and neutron scattering from polymers and considered a number of form factors. These included the simple spherical shapes as well as other geometrical shapes such as ellipsoidal, octahedral, and disks.

George and Wang considered turbulence as a space-time fractal grid process and demonstrate that the measured power spectrum exhibits a power law behavior, at least over three decades of scale (George and Wang 2009).

1.1.4. Fractal structures and scattering

Since the popular work by Mandelbrot (1977), the idea of self-similar structures occurring across a wide range of scales has been applied to natural structures. The concept of fractals in biological systems has seen numerous applications (Bassingthwaighte and Bever 1991, Glenny *et al* 1991). The nature of scattering from fractal structures has also received attention, with the concept of a fractal dimension d_f driving power law relations and scattering behavior. For 3D space-filling structures, the measured d_f would be less than 3. Lin *et al* (1989) modeled fractal aggregates and essentially argue that the long wavelength (low frequency or Rayleigh scattering) limit would be the standard k^4 dependence of backscatter where the wavenumber $k = \omega/c$, whereas the short wavelength (high frequency) limit would approach $k^{(4-d_f)}$. Javanaud (1989) simply invoked a power law relation for scattering using d_f as the scaling power.

Shapiro (1992) argued from a number of examples that a fractal structure would have a spectrum (over some range of scales) that follows a power law, and derived scattering formula for different regimes under that assumption. One conclusion was that over some scale the backscattered intensity would be proportional to $k^{(4+\nu)}$, where ν is a constant related to the fractal power law behavior. The compatibility of these works requires further study.

In summary, we are left with a set of theoretical correlation functions in random media that are related to exponentials, Gaussians, spheres, and rather loosely defined fractals that are linked to power law relations. This leaves open some remaining questions as to the structure and nature of backscatter from soft tissues.

2. Theory of soft tissue fluid channel scattering

2.1. General theory

When considering scattering from random media, it can be shown (Ishimaru 1978a, Campbell and Waag 1984b, Insana *et al* 1990) that the relationship between the differential scattering cross section per unit volume $\sigma_d(k)$ and the spatial correlation $b(\hat{r})$ function of the inhomogeneities is

$$\sigma_d(k) = k^4 A \iiint b(\hat{r})\, \mathbf{e}^{j2\hat{k}\cdot\hat{r}} dVol, \tag{1}$$

where k is the wavenumber and $\hat{r}$ is the vector separation between two points within the ensemble average. Assuming the correlation function is isotropic and simply dependent on separation distance r, the volume integral reduces to

$$VI(k) = \frac{2\pi}{k}\int_0^\infty r \cdot b(r) \sin(2kr)\, dr, \tag{2}$$

similar to the integral found in equations (4), (9) and (11) from Parker (2017) covering both acoustic and electromagnetic scattering under the Born approximation.

By comparing this to the form of the 3D Fourier transform in spherical coordinates shown in appendix A with spherical symmetry ${}^{3DS}\Im\{\}$ (Bracewell 1965, Baddour 2010) we may write

$$\sigma_d(k) = A \cdot k^4 \cdot {}^{3DS}\Im\{b(r), k\}, \tag{3}$$

where ${}^{3DS}\Im\{b(r), k\} = (2\pi/k)\int_0^\infty r \cdot b(r) \cdot \sin(2kr)\, dr$. Thus, the calculation of backscattering reduces to the question of the 3D Fourier transform of the isotropic and spherically symmetric ensemble-averaged correlation function of r. This spatial correlation function of cylindrical fluid-filled vessels is considered next.

2.2. Particular cylindrical shapes

We consider fractal branching networks of the fluid-filled vasculature and other parallel fluid channels as primary scattering sites. For example, the liver is highly vascularized (Guyton 1971) with both hepatic arterial and portal venous systems as well as the hepatic vein and the lymphatic, the biliary, and other fine scale extracellular paths, as shown in figure 1.

Hepatocytes form nearly 80% of the liver volume (Guyton 1971) and blood and fluid-filled vessels have a relative change in compressibility on the order of 3%, as described in appendix B.

Since soft tissue vascularity and fluid channels are considered to have a branching, self-similar, multi-scale, or fractal behavior, we consider a model of scattering, shown in figure 2, where the shapes are formed from long cylinders, branching and covering the 3D volume. The mathematics of this phenomenon have been actively studied and a key parameter is the distribution of vessels as a function of diameter. For example, larger vessels will branch into two or three smaller 'daughter' vessels and this continues over many scales or generations. The increasing number of vessels with smaller and smaller diameters has been shown to follow a power law function (Singhal

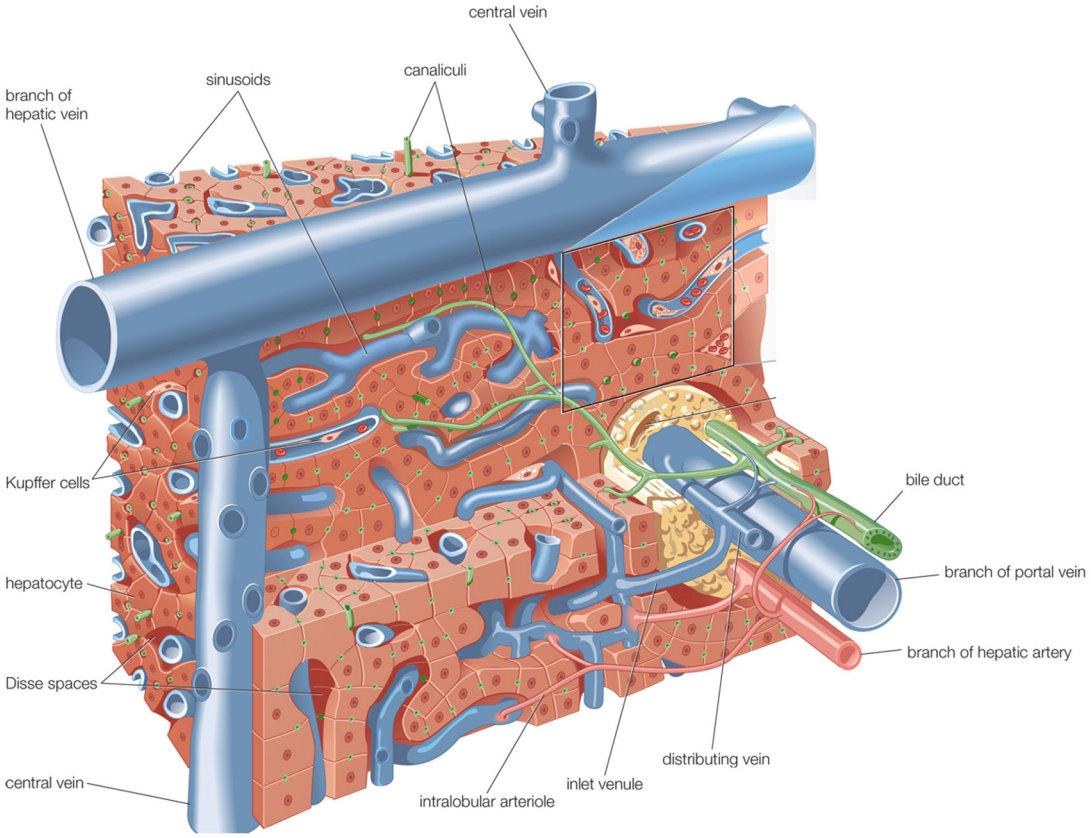

Figure 1. Complex architecture of the liver illustrating possible scattering sites and their range of sizes. By courtesy of Encylopaedia Britannica, Inc., copyright 2010; used with permission.

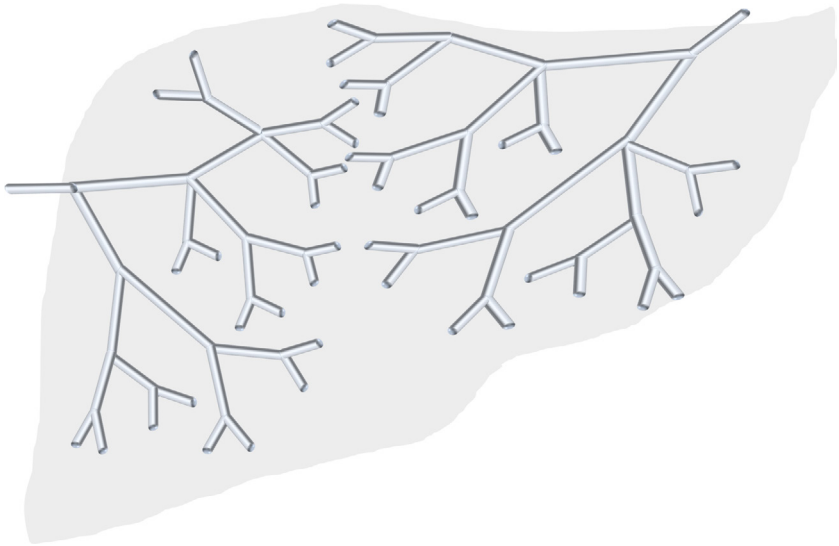

Figure 2. Schematic illustration of fractal branching vasculature elements as long cylindrical shapes within a soft tissue organ. The elements will be branching and self-similar over a wide range of diameters. Key assumptions include a branching pattern whereby the number of vessels at each diameter is governed by a power law, and that the ensemble average used to determine scattering behavior contains an approximately isotropic distribution of cylindrical shapes.

et al 1973, Krenz *et al* 1992, Gan *et al* 1993, Parker *et al* 1997) in different organs. Accordingly, for our scattering model we assume a continuous distribution of cylindrical diameters from large to small, following a power law: $N(a) = N_0/a^b$. The power law parameter b captures an important dimension of the fractal branching model; its relationship to other fractal measures is discussed in more detail in section 4.4. With reference to figure 2, we will also assume that the 3D region of interest interrogated for the ensemble average scattering measure will have a generally isotropic distribution of the cylindrical vessels. This assumption would not hold for anisotropic tissues such as muscles.

Assuming an isotropic spatial and angular distribution of each generation of fractal branching structures, the goal is to integrate the form of a basic element across all angles of incidence with respect to the interrogating ultrasound and across all size scales from very small microchannels of fluid to the largest arteries and veins that can exist within the organ. Specifically, we will examine four canonical cylindrical shapes as weak scattering primitives, in order to examine the range of backscatter versus frequency behavior that may be possible. In these formulations, $f(r)$ is the fractional change in incompressibility (and/or density) of the shape, r is the radial coordinate, and $F(\rho)$ is its Hankel transform with ρ as the spatial frequency. The four cylindrical scattering shapes are as follows.

(Case 1) The fluid-filled cylinder of radius a:

$$\begin{aligned} f(r) &= \begin{cases} \kappa_0 & r \leqslant a \\ 0 & r > a \end{cases} \\ F(\rho) &= \frac{\kappa_0 \cdot a \cdot J_1[2\pi a \cdot \rho]}{\rho}. \end{aligned} \tag{4}$$

(Case 2) The fluid 'cup' with strongly scattering walls of opposite sign:

$$\begin{aligned} f(r) &= \begin{cases} \kappa_0 \cdot \left(1 - 2\left(\frac{r}{a}\right)^2\right) & r \leqslant a \\ 0 & r > a \end{cases} \\ F(\rho) &= \frac{\kappa_0 \cdot a \cdot J_3[2\pi a\rho]}{\rho}. \end{aligned} \tag{5}$$

(Case 3) Cylindrical walls:

$$\begin{aligned} f(r) &= \kappa_0 \delta[r - a] \\ F(\rho) &= 2\pi\kappa_0 \cdot a \cdot J_0[2\pi a \cdot \rho]. \end{aligned} \tag{6}$$

(Case 4) Zero mean vessel with walls of opposite sign:

$$\begin{aligned} f(r) &= \kappa_0 \left[1 - \left(\frac{r}{a}\right)^2\right] \mathbf{e}^{-\left(\frac{r}{a}\right)^2} \\ F(\rho) &= a^4\pi^2\kappa_0\rho^2 \mathbf{e}^{-(a\pi\rho)^2}, \end{aligned} \tag{7}$$

where κ_0 is the fractional variation in density plus incompressibility, assumed to be $\ll 1$ consistent with the Born formulation. These four functions are displayed in figure 3.

We will work through the derivation and assumptions for Case 1, the fluid cylinder, and then summarize the results for the others and compare these.

First, assuming the fluid-filled cylinder is long in the z-axis, then the shape is 1D and its autocorrelation can be obtained from the inverse Hankel transform of the square of the shape's Hankel transform:

$$B_{cyl}(r) = 2\pi \int_0^\infty \rho \cdot F(\rho)^2 J_0(2\pi r \cdot \rho)\, d\rho, \tag{8}$$

where ρ is the spatial frequency. Second, we assume that cylinders of this kind exist within a fractal geometry in an isotropic pattern. Therefore, copies of this are interrogated by the forward wave over all possible angles. Thus, we form a 3D isotropic correlation function for the shape by conversion to spherical coordinates.

Consider first one infinitely long cylinder, with material property $f(r)$—symmetric—as shown in figure 4(a). It has a 3D transform that is a thin disk (delta function in k_z but shown with finite thickness to make the graphic easier to draw and visualize). Its transform in the k_x, k_y directions is symmetric and given by the Hankel transform of order zero, $F(\rho) = \mathcal{H}\{f(r), \rho\}$. A particular radius of value q_0 is shown for reference.

Now, if we measure an ensemble average of $F^2(\rho)$ across many cylinders at random angles (orientations) as shown in figures 4(c) and (d), but consider them as uniformly distributed with respect to angles (a cloud of sparsely spaced and randomly oriented scattering cylinders), then the ensemble average 3D transform is formed from the disk shown in figure 4(d), summing up over all realized angles. In the limit, any cylindrical radius q_0 in figure 4(b) forms a spherical shell in the ensemble average (figure 4(e)).

Thus, the ensemble average simply takes the Hankel transform function $F^2(\rho)$ found in figure 4(b) and populates the spherically symmetric 3D transform $B_s(q)$. However, there is a scaling of the cylindrical transform

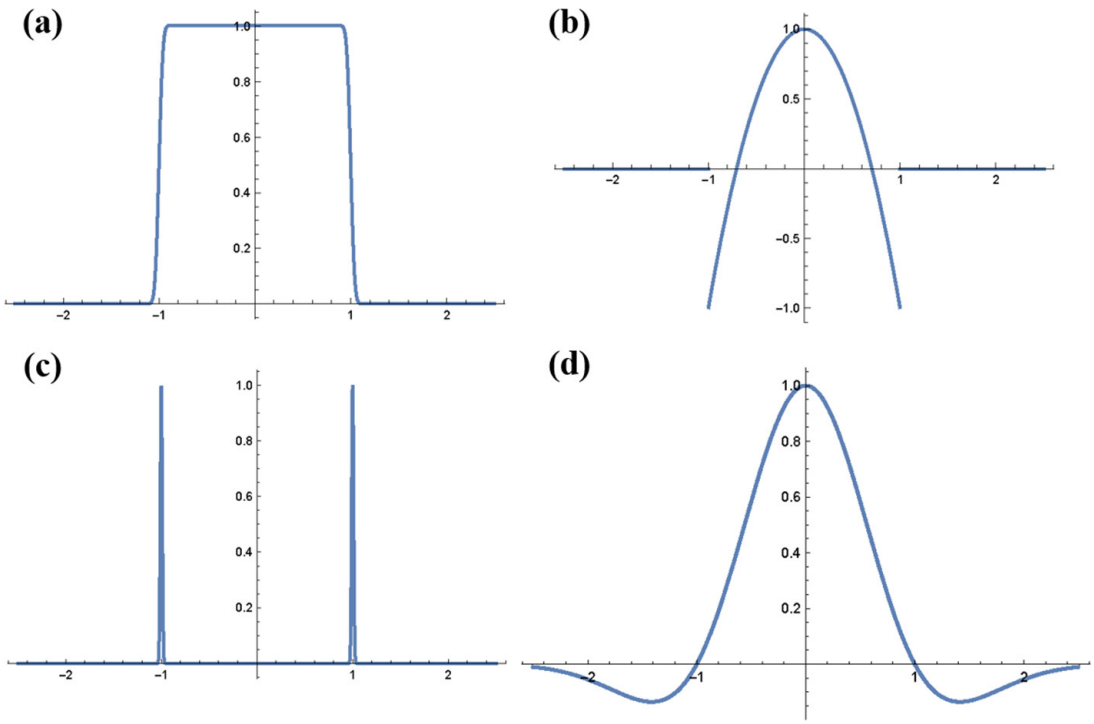

Figure 3. The four cylindrical shapes studied: (a) the fluid-filled cylinder, (b) the fluid cylinder with strongly scattering walls of opposite sign, (c) the cylindrical walls or shell, and (d) a modified Gaussian shape with walls of opposite sign. The vertical axis is the fractional inhomogeneity (arbitrary magnitude, see appendix B for estimates). The horizontal axis is r/a, normalized radial distance.

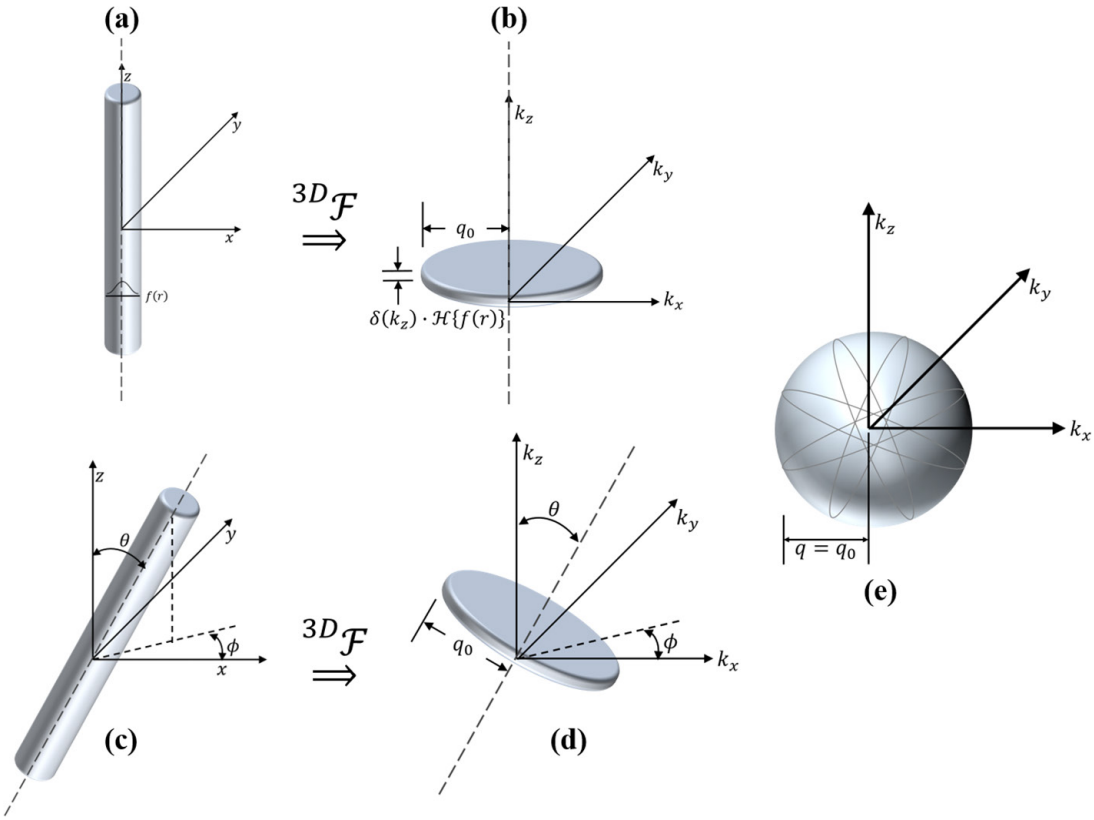

Figure 4. A cylindrical function (a) and its Hankel transform represented in 3D Fourier transform space (b). Rotations around spherical coordinates (c) similarly rotates the corresponding transform (d), leading to a spherically symmetric ensemble average (e).

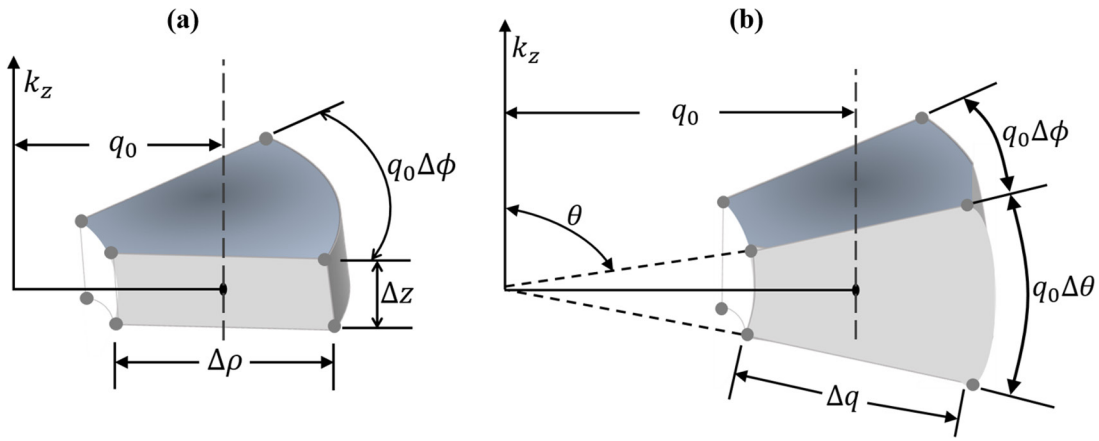

Figure 5. Differential volume element around point q_0 in 3D curvilinear coordinates; cylindrical coordinates in (a), and spherical coordinates in (b).

function over the spherical ensemble average. Specifically, the 3D spatial Fourier transform of the long cylinder can be expressed as

$$\begin{aligned} F^2\left(k_x, k_y, k_z\right) &= {}^{3DS}\Im\left\{b\left(r\right)\right\} \\ &= \delta\left(k_z\right)\mathcal{H}_0\left\{b\left(r\right), \rho\right\} \\ &= \delta\left(k_z\right)F^2\left(\rho\right) \end{aligned} \tag{9}$$

where $\rho^2 = k_x^2 + k_y^2$ and $\mathcal{H}_0\{\}$ is the Hankel transform of order zero (Bracewell 1965) and $\delta(\cdot)$ is the Dirac delta function. However, a thin disk (delta function) in cylindrical coordinates represented as $F^2(\rho_0)\,\delta(k_z)$ must be converted to a thin disk in spherical coordinates $B_s(q_0)\,\delta(\theta - \pi/2)$ as considered in figure 5, where the common radius $\rho_0 = q_0$ and $\Delta\rho = \Delta q$. Of importance is the relative scaling of the functions within the conversion to spherical coordinates.

In the limit of small element size, the integral of each function, or Riemann middle sum, around a point q_0 on a plane orthogonal to the k_z axis will be

$$\begin{matrix} q_0 \cdot F^2\left(q_0\right)\Delta\rho\Delta\phi & for & \text{Figure 5(a)} \\ q_0^2 \cdot B_s\left(q_0\right)\Delta q\Delta\phi & \text{for} & \text{Figure 5(b)'} \end{matrix} \tag{10}$$

where the sifting property of the Dirac delta function in curvilinear coordinates is used in the Δz and $\Delta\theta$ directions, respectively. In spherical coordinates, this result is independent of θ (see equation (17) of Baddour (2010)). By setting these equal and thus independent of coordinate system, and setting $\Delta\rho = \Delta q$, we find

$$B_s\left(q\right) = \frac{F^2\left(q\right)}{q}. \tag{11}$$

Thus, with reference to equation (3), we conclude that

$$\begin{aligned} \sigma_d\left(k\right) &= A \cdot k^4 \cdot {}^{3DS}\Im\left\{b\left(r\right), k\right\} \\ &= A \cdot k^4\left(\frac{F^2\left(k\right)}{k}\right) \\ &= Ak^3F^2\left(k\right), \end{aligned} \tag{12}$$

where $F^2(k) = \left(\mathcal{H}_0\left\{f\left(r\right), k\right\}\right)^2$.

Finally, the cross-correlation of an ensemble of these elements against all other (larger and smaller) elements within a fractal structure needs to be derived. The simplest assumption that can be made is that each scattering element has an autocorrelation function with itself that has been determined (equation (8)), but within the overall ensemble average the cross terms with all other branches (larger and smaller within the fractal structure) is simply a small constant that is essentially invariant with position and therefore can be neglected except for spatial frequencies nearing zero. Under that very simplistic assumption, the overall autocorrelation function within the ensemble is given by the principle of superposition as the sum (or integral in the continuous limit) of the different sizes' correlation functions over all generations of branches, weighted by their relative numbers (number density in the continuous limit). Fractal structures in 3D and volume filling in 3D tend towards number density functions that are represented by N_0/a^b, where a is the characteristic radius of the canonical element, N_0 is a global constant, and b is the power law (Krenz *et al* 1992). Within this framework, the overall correlation function $B_T(r_s)$ is

$$B_T(r_s) = \int_0^\infty N(a)\, B_s(r_s)\, da = \int_0^\infty \frac{N_0}{a^b} B_s(r_s)\, da \tag{13}$$

where $N(a)$ is the number density of elements as a function of size a. Alternatively, in the 3D transform domain:

$$B_{TR}(k) = \int_0^\infty N(a)\left[F_r^2(k,a)/k\right] da. \tag{14}$$

For the specific Case 1, the fluid cylinder, this becomes

$$B_{TR}(k) = \int_0^\infty \left(\frac{N_0}{a^b}\right)\left(\frac{1}{k}\right)\left(\frac{\kappa_0 a J_1[2\pi a k]}{k}\right)^2 da = f_1(b)\, k^{(b-6)} \quad \text{for} \quad 2 < b < 3, \tag{15}$$

where $f_1(b)$ is a function of b. Thus, with reference to equation (3), we conclude that for Case 1:

$$\sigma_d(k) = A f_1(b)\, k^{(b-2)}. \tag{16}$$

Note that the integral operators (transform, average over angles, average over radii) are all linear so the order of these operations can be transposed for computational ease.

Our general approach is shown in figure 6.

3. Results

The four functions shown in figure 3, plus a range of others with plausible corresponding shapes comprised of exponential, Gamma, and modified Bessel functions of integer order (Parker 2018), were treated in accordance to the procedure shown in figure 6. As shown in table 1, with one exception, the results are uniform in predicting that $\sigma_d(k)$ will be proportional to the power $b-2$, in the range of convergence usually $b < 5$. The exception is Case 3 with the delta function wall, resulting in scattering proportional to the power b. This, however, assumes that the scattering delta function has a strength of κ_0 throughout, invariant with scale. If we instead assume that the delta function magnitude is proportional to an invariant κ_0 times a small thickness proportional to a, then this function, rotated and scaled, reverts to the $b-2$ power which is common to the other tested functions. Other power laws can be generated from arbitrary functions in $f[r]$, particularly when singularities at the origin are considered, such as $1/r$ or $\log[r]$ functions; however these would be difficult to justify in terms of the physical structure of fluids within a long vessel.

4. Discussion

4.1. Assessment of the model versus measured data

For soft tissue scattering, a number of studies have linked optical and acoustical measurements of tissue specimens. Looking at backscatter results from soft tissues, we see that most of the carefully calibrated systems report smoothly increasing backscatter with frequency. Generally this can be fit to a power law with an exponent of $1 < \gamma < 2$ for liver, with some tissues' power law estimate at $2 < \gamma < 3$ (see figure 6.6 in Hill *et al* (2004), table 4.22 in Duck (1990), and table 1 in Nasief *et al* (2015)). For example, Campbell and Waag found liver backscatter to increase as $f^{1.4}$ over the medical imaging band of 3–7 MHz (Campbell and Waag 1984a) consistent with other pioneering reports from the early 1980s (Reid and Shung 1979, Bamber and Hill 1981, Nicholas 1982, Lizzi *et al* 1983, D'Astous and Foster 1986).

Although many scattering studies were performed on *ex vivo* specimens that were carefully procured and prepared so as to minimize artifacts, some early *in vivo* studies also produced results that were consistent with the *ex vivo* measurements (Zagzebski *et al* 1993, Wear *et al* 1995, Lu *et al* 1997, 1999) from different groups.

To compare theory and experiments, we replicate data from liver backscatter from Campbell and Waag (1984a) at discrete frequencies from 2 to 7 MHz, these are shown as blue dots in figures 7(a) and (b), converted to wavenumber assuming the speed of sound is 1.5×10^6 mm s^{-1}. Also shown are the formulas for Case 1 (top, blue line), Case 4 (middle, green) and Case 2 (lowest line, red), assuming nominal parameters of $\kappa = 0.05$, $N = 1/2000$, and $b = 3.4$, which according to table 1 produces a scattering power law proportional to frequency to the power 1.4, noted by Campbell and Waag at that time. This shows reasonable agreement; however the value of $b = 3.4$ is above the upper limit of convergence of the integral over all cylindrical diameters a from 0 to infinity (see equations (13)–(15)). This can be avoided with practical, finite limits on the integration and, so long as a reasonable number of decades of diameters are included, the predicted power law is still observed. For example, figure 7(b) uses numerical integration of Case 1, equation (15), with limits of integration on $a = \{4$ microns, 1 mm$\}$, and similarly a numerical integration over the same limited range for Case 2 and Case 4. In these cases, the power law coefficient of 1.4 is still observed up to the higher wavenumbers, where the integrand is sensitive to the lower limit of diameters entered.

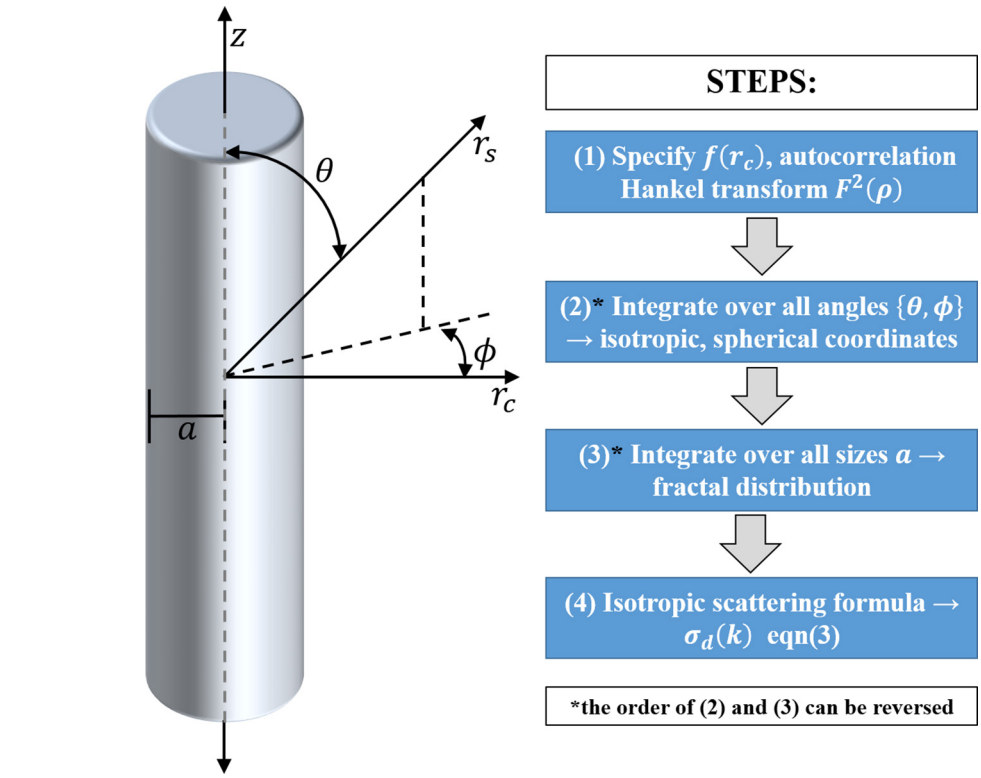

Figure 6. Derivation of isotropic scattering from cylindrical element of radius a, where r_c is the radial coordinate in cylindrical coordinates and r_s in spherical coordinates.

Table 1. Scattering functions.

	Inhomogeneity shape	Ensemble average	Backscatter
Function	$f(r)$	$\int_0^\infty \frac{1}{a^b}\left(\frac{F^2(q)}{q}\right)da$	$\sigma_s(k)$
Case 1	$\kappa_0 \quad r \leqslant a$ $0 \quad r > a$	$f_1(b)\, q^{(b-6)}$	$c_1 k^{(b-2)}$
Case 2	$\kappa_0\left(1-2\left(\frac{r}{a}\right)^2\right) \quad r \leqslant a$ $0 \quad r > a$	$f_2(b)\, q^{(b-6)}$	$c_2 k^{(b-2)}$
Case 3	$\kappa_0 \delta(r-a)$	$f_3(b)\, q^{(b-4)}$	$c_3 k^{(b)}$
Case 4	$\kappa_0\left[1-\left(\frac{r^2}{a^2}\right)^2\right]\mathrm{e}^{-\left(\frac{r}{a}\right)^2}$	$f_4(b)\, q^{(b-6)}$	$c_4 k^{(b-2)}$

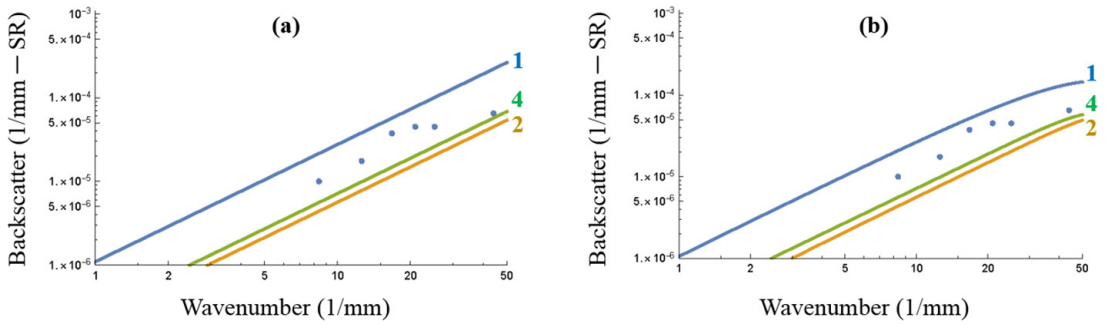

Figure 7. (a) Theoretical versus experimental backscatter versus wavenumber using values from Campbell and Waag (1984a) for *ex vivo* calf liver (dots) as compared with theory. Solid lines are, from upper to lower: Case 1, fluid-filled cylinder with $\kappa = 0.05$, Case 4 modified Gaussian radial shape, Case 2 parabolic radial shape. (b) uses the same data and cases, except numerical integration was used over a practical range of diameters, $a = \{0.04, 1\}$ mm instead of $a = \{0, \text{infinity}\}$. The power law coefficient of 1.4 noted by Campbell and Waag is still observed over most of the range despite the truncated limits of integration. For reference, a wavenumber of 20 corresponds to approximately 5 MHz, within the range of adult liver scans.

Other examples of increasing backscatter versus frequency can be seen in figure 5 of Ghoshal *et al* (2012) extending up to 25 MHz in liver, and in figure 5 of Lu *et al* (1999), also in livers. Similarly, for other tissues including sarcoma and carcinoma models, see figure 7 of Oelze and Zachary (2006), and for thyroids, see figure 4 of

Rouyer *et al* (2016). Thus, in assessing our theoretical models we are seeking a prediction of a backscatter power law fit of an exponent larger than or equal to 1.4 in liver, given a relatively isotropic fractal fluid network scattering power law of $b-2$. In that case, it is clear that the power law b governing the number density of vessels must be greater than 3. This is plausible, although reported data has to be considered in light of the methodologies used; this will be considered in section 4.4. We also note for completeness that for $F[q]^2/q$ in spherical radial frequency being proportional to $q^{(b-6)}$, also corresponds in the spatial domain to an autocorrelation function proportional to $1/r_s^{(b-3)}$, where $3 < b < 5$. In other words, a power law in scattering is produced by a power law in spatial autocorrelation of the weak cylindrical inhomogeneities.

4.2. Limits of integration

One possibly unrealistic feature of these derivations is that the integration over diameters a has been taken from zero to infinity, meaning small to large diameter cylinders without specifying realistic limits on each end. It should be noted that in all the functions examined (and other well behaved functions) the results are only weakly dependent on the exact limits so long as the limits cover many decades of scale above and below the midband of the medical ultrasound range (single digit MHz range). This behavior is demonstrated in figure 7(b). However, the exact limits in soft, vascularized tissue are of interest, especially as higher frequency systems become available for small parts and small animal imaging. At the low end, Schmitt and Kumar (1996) studied phase contrast images of mouse liver histology slides and found a power law power spectrum behavior for spatial frequencies down to at least 1/10 microns^{-1} (see figure 8).

Similarly, Rouyer *et al* (2016) studied thyroid tissue and by replotting their data we can estimate a power law behavior from 6 MHz to 16 MHz, corresponding to wavelengths as low as 90 microns.

We note that of the evaluated models, two have a zero mean $f(r)$, corresponding to an important theoretical issue of a zero mean $F(\rho = 0)$. This was addressed by Waag *et al* (1989b), who noted that 'The additional assumption of weak scattering is required so that the Born approximation holds. Then the condition of zero spectral power at a spatial frequency value of zero follows directly from consideration of the mean-square value of scattered pressure at zero spatial frequency when the scattered pressure is expressed as a spatial Fourier transform of the medium variations which are defined to have a zero mean value'. In other words, the entire framework of the Born approximation assumes a fractional, zero mean variation in density and compressibility, thus the Fourier transform (related to backscatter versus frequency) must approach zero at zero spatial frequency. In our examples, Cases 2 and 4 (figures 3(b) and (d)) explicitly have that property. The physical interpretation would be that the extracellular fluid resides within the channels, and the cellular structures forming the walls are of opposite fractional variation while the integration across the entire structure is set to zero mean.

Switching to the upper end of the integration over cylindrical scatterers of radius a, we note that ultrasound imaging of human abdomens at 3 MHz usually resolves individual hepatic arteries and vessels over a few millimeters in diameter; these may be 'cropped out' of the analysis in many ensemble averages. Thus, there is a practical limit on the upper end, and depending on the protocol used, this could alter the integration of equation (13) away from the assumed limits.

4.3. Modifications of the model

This paper has purposefully focused on normal vascularized tissues, to propose a model for the dominant structures defining backscatter. Of course, most diagnostic scans are done to assess the presence or absence of pathologies, so the next question pertains to how this fluid-channel fractal-network model would be altered by common disease states. One change in the model parameter that can easily be altered is the size distribution $N(a)$, which is related to the fractal dimension of the structures. Two opposites could be realized in different pathologies. For example, in some tumors the neovasculature, the leaky vasculature, and the elevated hydrostatic pressure could change the fractal properties of small (capillary-sized and smaller) fluid spaces compared with normal tissue (Savage *et al* 2013). Conversely, in early liver fibrosis the development of fibrotic structures larger than the hepatic sinusoids would increase the number density of larger structure sizes, relative to normal tissue. These can be modeled to some extent by changes in $N(a)$ and specifically the power law. In turn, this increases or decreases the slope of the backscatter versus frequency curve.

However, there may also be pathologies where the scattering model must also consider spherical shapes in addition to the cylindrical fluid spaces. Liver steatosis would be one prominent example as the subcellular-sized spherical fat vacuoles accumulate and may be modeled as Rayleigh scatterers over some frequency range (Parker 2016, Parker *et al* 2018). In this case, the total scattering would result from both the fractal network of fluid branches and the Rayleigh spherical scatterers, thus exhibiting a power law plus f^4 behavior. Furthermore, even in normal tissues, cellular inhomogeneities such as mitochondria could have a scattering effect. Given the size of sub-cellular components, these would also produce Rayleigh f^4 contributions over the usual clinical range of frequencies. There is an ironic historical twist to this concept since over 70 years ago Mason and McSkimin (1947) proposed a dual model for scattering and attenuation from metal and glass samples, with a linear function (power law near 1) plus an f^4 Rayleigh term.

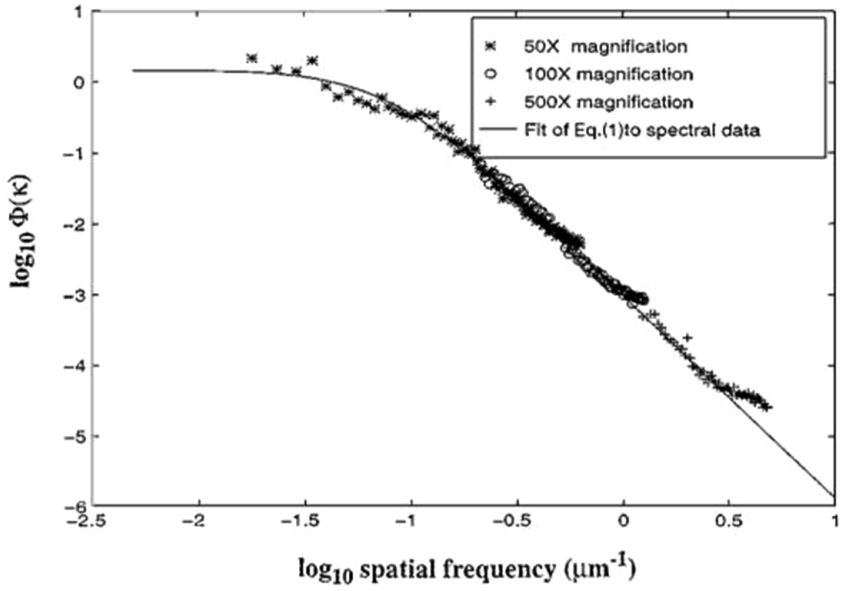

Figure 8. Optical scattered power spectrum of tissue slides indicating a power law behavior to below 0.1 microns in scale. Reprinted with permission from Schmitt and Kumar (1996), OSA Publishing.

4.4. Refinement of theory versus experiments

Further experimental results over an extended frequency range are required to test the proposed cylindrical model of fluid channels in fractal networks, in competition with earlier models based on spherical cell shapes. It would be valuable to have data on normal vascularized tissues over a wide bandwidth so that baseline measures could be established and hypothesis testing (cylindrical versus spherical) could be accomplished with a high degree of confidence.

A more exact comparison of theory to experiment will require greater precision on two fronts: the scattering power law, and the fractal branching power law of the fluid channels for specific organs. In order to obtain system-independent values of tissue backscatter, experimental measures must carefully consider the beam width and axial window employed, along with the transducer round trip sensitivity as a function of frequency. The type of system correction depends on the approach taken. For example, Campbell and Waag (1984a, 1984b) and Davros *et al* (1986) employed separate transmit and receive transducers, so the beam's overlap in space was calculated as a function of frequency and angle. The quantitative approach developed by Lizzi *et al* (1983) employed a reference spectrum approach and beampattern terms. The reference phantom or reference scatterer approach (Yao *et al* 1990, Wear *et al* 1995, Chen *et al* 1998) utilizes a well characterized set of scatterers, usually small Rayleigh scatterers, scanned at the same depth and same system settings as the tissue, to provide the correction for system-dependent effects.

The fractal branching behavior assumed in equation (13) is a continuous number density of cylinders represented as proportional to $1/a^b$; this forms a major assumption of this framework, yet is not known precisely. In reviewing the literature results, it must be kept in mind that there are major distinctions running through different analyses, principally 2D versus 3D, and also the type of measurement utilized. Fractal dimension is limited by topographical dimension, so 2D analysis of slices or projections will have a lower dimension than corresponding 3D measurements. Full 3D measurements at high resolution are rare and difficult due to the demands on resolution and sheer size of the imaging data. Some high quality and high resolution 3D assessments of the branching vasculature have been painstakingly acquired for the brain (Risser *et al* 2007) and the placenta (Parker *et al* 2016), however to our knowledge there have not been any published results from 3D fractal analyses of the liver, prostate, or thyroid vasculature at high resolution.

Adding to the uncertainty about the important power law parameter b, which defines the number density of cylindrical vessels as a function of their radius, over the ensemble and in linear dimensions, is the wide variety of measurement styles that are typically reported. This is a major source of possible misinterpretation. Our power law parameter b is not the same as the fractal dimension measured by sandbox or related box counting techniques. Even in the cases of older literature reports where the number of vessels were painstakingly counted (see figure 1 of Krenz *et al* (1992) indicating a power law of approximately -2.7 over some older studies, or table 1 of Gan *et al* (1993) indicating a power law of approx. -1.3 in pulmonary veins, or table 4 of Singhal *et al* (1973) suggesting a power law of -2.5 in pulmonary arteries), there are important methodological details that can swing the assessment. For example, many counting schemes derive the number of vessels versus branch generation number 1,2,3,… as ordinal numbers. The slope of this curve is not the same as our number density versus radius

curve. Other schemes count 'greater than or equal to' a varying radius, which corresponds to an integration. Since the integration of $1/a^b$ is proportional to $1/a^{(b-1)}$, this scheme inherently shifts and reduces the power law parameter by one. Similarly, a scheme of 'binning' together vessels by proportional limits over a log scale will shift the power law. For example, counting all the vessels within $\pm$15% of 0.1 mm, then all those within 15% of 1 mm, then all those within 15% of 10 mm, will effectively integrate the distribution within these bins, again converting the continuous distribution to a discrete set with $1/a^{(b-1)}$ relative distribution. For all these reasons, it is plausible that different literature reports of branching vascular number densities will vary depending on the methodology used. Clearly, high-resolution data sets in 3D are required to better define this important factor in soft tissues such as liver, thyroid, prostate, and others.

4.5. Limitations of the model

This scattering model assumes that the dominant tissue parenchyma, for example the hepatocytes in the liver, form the reference media and the cylindrical-shaped vasculature and fluid channels form the scattering sites. As such, the canonical shape is a long cylinder, and the fractal branching structure is assumed to conform to a power law distribution of radii over many decades of sizes (many small cylinders and fewer large cylinders). It is further assumed that an ensemble average incorporates orientations of all cylinders across all angles. This limits the model to relatively isotropic tissues and would require modifications to address oriented structures such as myocardial muscle. Furthermore, the exact branching conditions of termination (connection) and branching angle are not explicitly considered and require further study. Finally, it is assumed that the cross correlation of each long cylindrical segment with all others is a relatively small and nearly constant parameter across spatial correlation lags, limiting the importance of this term to very low frequencies in practice. Within this simplified framework a power law of scattering is predicted based on the power law distribution of vessel sizes. 3D vasculature studies at high resolution are now required in parallel with quantitative scattering measurements to more fully assess the predictions and limits of applicability of the proposed model.

5. Conclusion

A hypothesis about scattering from tissue is generated from primitive cylindrical shapes representing the plausible distribution of extracellular fluids and blood in long fluid-filled channels throughout normal soft tissue. Assuming a wide range of diameters of the cylindrical fluid spaces and an isotropic distribution, the predicted backscatter is of the form of a power law with dimension greater than one. This matches some observations about the nature of vessels and measurements of backscatter from tissues such as the liver and thyroid. The theory, then, represents an alternative to longstanding explanations of scattering linked to properties of spheres representing cells. In the cylindrical fluid model, the fluid-filled vasculature and channels are the scattering sites, whereas the close-packed cells form the reference media. Pathologies that affect tissue morphology would be expected to modify this model in significant ways, but it is prudent to first establish an accurate working model of normal soft tissue scattering. More precise measurements of the key parameters will be required to fully test this hypothesis and prior models based on spheres.

Acknowledgments

This work was supported by the Hajim School of Engineering and Applied Sciences at the University of Rochester and National Institutes of Health Grant No. R21EB025290. The author is deeply appreciative of comments and perspectives on earlier versions of this manuscript from Prof N Baddour and Dr J Astheimer, and is grateful for the insights gained from the pioneering work of Prof R Waag, the late Prof R Chivers, the late Prof F Lizzi, and their colleagues.

Appendix A. Particular form of Fourier transform pairs

Consistent with Bracewell (1965), we use the following convention.

(a) Fourier transform in one dimension:

$$\begin{aligned} F(s) &= \int_{-\infty}^{\infty} f(x)\, \mathbf{e}^{-i2\pi xs} dx = \Im\{f(x)\} \\ f(x) &= \int_{-\infty}^{\infty} F(s)\, \mathbf{e}^{+i2\pi xs} ds. \end{aligned} \tag{A.1}$$

(b) Fourier transform/Hankel transform for cylindrical symmetry:

$$\begin{array}{c} F(\rho) = 2\pi \int_0^\infty f(r)\, J_0(2\pi\rho r)\, rdr = \mathcal{H}\{f(r)\} \\ f(r) = 2\pi \int_0^\infty F(\rho)\, J_0(2\pi\rho r)\, \rho d\rho. \end{array} \tag{A.2}$$

(c) 3D Fourier transform with spherical symmetry:

$$\begin{array}{c} F(q) = \frac{2\pi}{q} \int_0^\infty f(r) \sin(2qr)\, rdr = {}^{3DS}\Im\{f(r)\} \\ f(r) = \frac{2\pi}{r} \int_0^\infty F(q) \sin(2qr)\, qdq. \end{array} \tag{A.3}$$

Within this convention, the transform variable has units of cycles/distance. Furthermore, the 3D spherical transform is identical to the kernel for Born scattering, equations (1)–(3).

Appendix B. Estimates of inhomogeneities

We examine compressibility κ as a source of scattering where $\kappa = 1/c^2\rho$, c is compressional wave speed, and density $\rho \cong 1\,\mathrm{kg\,m^{-3}}$, and estimate the normalized fraction $\Delta\kappa/\kappa_0$ for blood plasma and whole blood compared to liver tissue from published studies of ultrasound speed of sound (Goss *et al* 1978, 1980, Duck 1990):

$$\begin{array}{rl} \text{For whole blood}: & \kappa_b = \frac{1}{(1575)^2(1055)} = 0.38\,(1/\mathrm{GPa}) \\ \text{For liver tissue}: & \kappa_l = \frac{1}{(1590)^2(1060)} = 0.37\,(1/\mathrm{GPa})\,. \end{array} \tag{A.4}$$

Then

$$\text{For whole blood}: \quad \frac{\Delta\kappa}{\kappa_l} = \frac{\kappa_b - \kappa_l}{\kappa_l} = 0.03 \text{ or } 3\% \text{ difference.} \tag{A.5}$$

This is without any assumptions about arterial or venous walls adding to the mismatch. The 3% difference is significant within the expected range of soft tissue inhomogeneities (Macovski 1983) and will be present in every major vessel containing whole blood or extracellular fluids. This 3% difference is also larger than the change in acoustic impedance assumed in 3D models of scattering from tissue (Mamou *et al* 2008) where values of 1.51/1.50 MRayls were used, a 0.6 % difference. Small capillaries and extracellular spaces may contain fluid that is not whole blood. Reported values of plasma have a lower speed (1520 m s^{-1}) than whole blood at 45% hemocrit (1575 m s^{-1}) (Goss *et al* 1978, 1980, Duck 1990), so these smaller cylinders would have a higher relative inhomogeneity, possibly boosting their relative contribution to the overall ensemble.

ORCID iDs

K J Parker https://orcid.org/0000-0002-6313-6605

References

Agterberg F P 1970 *Geostatistics: a Colloquium* ed D F Merriam (Berlin: Springer) pp 113–41
Baddour N 2010 Operational and convolution properties of three-dimensional Fourier transforms in spherical polar coordinates *J. Opt. Soc. Am.* A **27** 2144–55
Bamber J C and Hill C R 1981 Acoustic properties of normal and cancerous human liver—I. Dependence on pathological condition *Ultrasound Med. Biol.* **7** 121–33
Bassingthwaighte J B and Bever R P 1991 Fractal correlation in heterogeneous systems *Physica* D **53** 71–84
Born M and Wolf E 1980 *Principles of Optics: Electromagnetic Theory of Propagation, Interference and Diffraction of Light* (Oxford: Pergamon) pp 556–92
Bracewell R N 1965 *The Fourier Transform and its Applications* (New York: McGraw-Hill) ch 12
Campbell J A and Waag R C 1984a Measurements of calf liver ultrasonic differential and total scattering cross sections *J. Acoust. Soc. Am.* **75** 603–11
Campbell J A and Waag R C 1984b Ultrasonic scattering properties of three random media with implications for tissue characterization *J. Acoust. Soc. Am.* **75** 1879–86
Chen J F, Zagzebski J A, Dong F and Madsen E L 1998 Estimating the spatial autocorrelation function for ultrasound scatterers in isotropic media *Med. Phys.* **25** 648–55
Chernov L A 1960 *Wave Propagation in a Random Medium* (New York: McGraw-Hill)
Chivers R C 1977 The scattering of ultrasound by human tissues-some theoretical models *Ultrasound Med. Biol.* **3** 1–13
Cramblitt R M and Parker K J 1999 Generation of non-Rayleigh speckle distributions using marked regularity models *IEEE Trans. Ultrason. Ferroelectr. Freq. Control* **46** 867–74

D'Astous F T and Foster F S 1986 Frequency dependence of ultrasound attenuation and backscatter in breast tissue *Ultrasound Med. Biol.* **12** 795–808
Davros W J, Zagzebski J A and Madsen E L 1986 Frequency-dependent angular scattering of ultrasound by tissue-mimicking materials and excised tissue *J. Acoust. Soc. Am.* **80** 229–37
Debye P and Bueche A M 1949 Scattering by an inhomogeneous solid *J. Appl. Phys.* **20** 518–25
Debye P, Anderson H R Jr and Brumberger H 1957 Scattering by an inhomogeneous solid. II. The correlation function and its application *J. Appl. Phys.* **28** 679–83
Duck F A 1990 *Physical Properties of Tissues: a Comprehensive Reference Book* (Burlington, VA: Elsevier)
Faran J J Jr 1951 Sound scattering by solid cylinders and spheres *J. Acoust. Soc. Am.* **23** 405–18
Fellingham L L and Sommer F G 1984 Ultrasonic characterization of tissue structure in the *in vivo* human liver and spleen *IEEE Trans. Sonics Ultrason.* **31** 418–28
Gan R Z, Tian Y, Yen R T and Kassab G S 1993 Morphometry of the dog pulmonary venous tree *J. Appl. Physiol.* **75** 432–40
George W K and Wang H 2009 The exponential decay of homogeneous turbulence *Phys. Fluids* **21** 025108
Ghoshal G, Lavarello R J, Kemmerer J P, Miller R J and Oelze M L 2012 *Ex vivo* study of quantitative ultrasound parameters in fatty rabbit livers *Ultrasound Med. Biol.* **38** 2238–48
Glenny R W, Robertson H T, Yamashiro S and Bassingthwaighte J B 1991 Applications of fractal analysis to physiology *J. Appl. Physiol.* **70** 2351–67
Goss S A, Johnston R L and Dunn F 1978 Comprehensive compilation of empirical ultrasonic properties of mammalian-tissues *J. Acoust. Soc. Am.* **64** 423–57
Goss S A, Johnston R L and Dunn F 1980 Compilation of empirical ultrasonic properties of mammalian tissues. II *J. Acoust. Soc. Am.* **68** 93–108
Guyton A C 1971 *Textbook of Medical Physiology* (Philadelphia, PA: Saunders)
Hill C R 2004 *Physical Principles of Medical Ultrasonics* (Chichester: Wiley)
Insana M F and Brown D G 1993 *Ultrasonic Scattering in Biological Tissues* ed K K Shung and G A Thieme (Boca Raton, FL: CRC Press) pp 75–124
Insana M F, Wagner R F, Brown D G and Hall T J 1990 Describing small-scale structure in random media using pulse-echo ultrasound *J. Acoust. Soc. Am.* **87** 179–92
Insana M F, Wagner R F, Garra B S, Brown D G and Shawker T H 1986 Analysis of ultrasound image texture via generalized Rician statistics *Opt. Eng.* **25** 743–8
Ishimaru A 1978a *Wave Propagation and Scattering in Random Media* (New York: Academic)
Ishimaru A 1978b *Wave Propagation and Scattering in Random Media. Vol. 1. Single Scattering and Transport Theory* (New York: Academic)
Javanaud C 1989 The application of a fractal model to the scattering of ultrasound in biological media *J. Acoust. Soc. Am.* **86** 493–6
Krenz G S, Linehan J H and Dawson C A 1992 A fractal continuum model of the pulmonary arterial tree *J. Appl. Physiol.* **72** 2225–37
Landini L and Verrazzani L 1990 Spectral characterization of tissues microstructure by ultrasounds: a stochastic approach *IEEE Trans. Ultrason. Ferroelectr. Freq. Control* **37** 448–56
Lin M Y, Lindsay H M, Weitz D A, Ball R C, Klein R and Meakin P 1989 Universality of fractal aggregates as probed by light scattering *Proc. R. Soc.* A **423** 71–87
Lizzi F L, Greenebaum M, Feleppa E J, Elbaum M and Coleman D J 1983 Theoretical framework for spectrum analysis in ultrasonic tissue characterization *J. Acoust. Soc. Am.* **73** 1366–73
Lu Z F, Zagzebski J A and Lee F T 1999 Ultrasound backscatter and attenuation in human liver with diffuse disease *Ultrasound Med. Biol.* **25** 1047–54
Lu Z F, Zagzebski J A, O'Brien R T and Steinberg H 1997 Ultrasound attenuation and backscatter in the liver during prednisone administration *Ultrasound Med. Biol.* **23** 1–8
Machado C B, de Albuquerque Pereira W C, Meziri M and Laugier P 2006 Characterization of *in vitro* healthy and pathological human liver tissue periodicity using backscattered ultrasound signals *Ultrasound Med. Biol.* **32** 649–57
Macovski A 1983 *Basic Ultrasonic Imaging* (Englewood Cliffs, NJ: Prentice-Hall) ch 5
Mamou J and Oelze M L 2013 *Quantitative Ultrasound in Soft Tissues* (Berlin: Springer)
Mamou J, Oelze M L, O'Brien W D Jr and Zachary J F 2008 Extended three-dimensional impedance map methods for identifying ultrasonic scattering sites *J. Acoust. Soc. Am.* **123** 1195–208
Mandelbrot B B 1977 *Fractals: Form, Chance, and Dimension* (San Francisco, CA: W.H. Freeman)
Mason W P and McSkimin H J 1947 Attenuation and scattering of high frequency sound waves in metals and glass *J. Acoust. Soc. Am.* **19** 464–73
Morse P M and Ingard K U 1987 *Theoretical Acoustics* (Princeton, NJ: Princeton University Press) ch 8
Nasief H G, Rosado-Mendez I M, Zagzebski J A and Hall T J 2015 Acoustic properties of breast fat *J. Ultrasound Med.* **34** 2007–16
Nicholas D 1982 Evaluation of backscattering coefficients for excised human tissues: results, interpretation and associated measurements *Ultrasound Med. Biol.* **8** 17–28
Oelze M L and Zachary J F 2006 Examination of cancer in mouse models using high-frequency quantitative ultrasound *Ultrasound Med. Biol.* **32** 1639–48
Parker J C, Cave C B, Ardell J L, Hamm C R and Williams S G 1997 Vascular tree structure affects lung blood flow heterogeneity simulated in three dimensions *J. Appl. Physiol.* **83** 1370–82
Parker K J 2016 The H-scan format for classification of ultrasound scattering *J. OMICS Radiol.* **5** 1000236
Parker K J 2017 Hermite scatterers in an ultraviolet sky *Phys. Lett.* A **381** 3845–8
Parker K J 2018 The Hankel transform (www.hajim.rochester.edu/ece/sites/parker/hankel-transform/index.html)
Parker K J, Ormachea J, Drage M G, Kim H and Hah Z 2018 The biomechanics of simple steatosis and steatohepatitis *Phys. Med. Biol.* **63** 105013
Parker K J, Ormachea J, McAleavey S A, Wood R W, Carroll-Nellenback J J and Miller R K 2016 Shear wave dispersion behaviors of soft, vascularized tissues from the microchannel flow model *Phys. Med. Biol.* **61** 4890
Pedersen J S 1997 Analysis of small-angle scattering data from colloids and polymer solutions: modeling and least-squares fitting *Adv. Colloid Interface Sci.* **70** 171–210
Rayleigh L 1897 XXXVII. On the passage of waves through apertures in plane screens, and allied problems *Philos. Mag.* **43** 259–72
Rayleigh L 1918 On the scattering of light spherical shells, and by complete spheres of periodic structure, when the refractivity is small *Proc. R. Soc.* A **94** 296–300
Rayleigh L 1945 *The Theory of Sound: in 2 Volumes* (New York: Dover)

Reid J M and Shung K K 1979 Quantitative measurements of scattering of ultrasound by heart and liver *Ultrasonic Tissue Characterization II, Special Publication 525* ed M Linzer (Washington, DC: National Bureau of Standards., U.S. Government Printing Office) pp 153–6
Risser L, Plouraboue F, Steyer A, Cloetens P, Le Duc G and Fonta C 2007 From homogeneous to fractal normal and tumorous microvascular networks in the brain *J. Cerebr. Blood Flow Metab.* **27** 293–303
Rosado-Mendez I M, Drehfal L C, Zagzebski J A and Hall T J 2016 Analysis of coherent and diffuse scattering using a reference phantom *IEEE Trans. Ultrason. Ferroelectr. Freq. Control* **63** 1306–20
Rouyer J, Cueva T, Yamamoto T, Portal A and Lavarello R J 2016 *In vivo* estimation of attenuation and backscatter coefficients from human thyroids *IEEE Trans. Ultrason. Ferroelectr. Freq. Control* **63** 1253–61
Savage V M, Herman A B, West G B and Leu K 2013 Using fractal geometry and universal growth curves as diagnostics for comparing tumor vasculature and metabolic rate with healthy tissue and for predicting responses to drug therapies *Discrete Continuous Dyn. Syst. Ser.* B **18** 1077–108
Schmitt J M and Kumar G 1996 Turbulent nature of refractive-index variations in biological tissue *Opt. Lett.* **21** 1310–2
Shapiro S A 1992 Elastic waves scattering and radiation by fractal inhomogeneity of a medium *Geophys. J. Int.* **110** 591–600
Sheppard C J R and Connolly T J 1995 Imaging of random surfaces *J. Mod. Opt.* **42** 861–81
Shung K K and Thieme G A 1993 *Ultrasonic Scattering in Biological Tissues* (Boca Raton, FL: CRC Press)
Singhal S, Henderson R, Horsfield K, Harding K and Cumming G 1973 Morphometry of the human pulmonary arterial tree *Circ. Res.* **33** 190–7
Tatarskii V I 1961 *Wave Propagation in a Turbulent Medium* (New York: McGraw-Hill)
Varghese T and Donohue K D 1993 Characterization of tissue microstructure scatterer distribution with spectral correlation *Ultrason. Imaging* **15** 238–54
Waag R C, Dalecki D and Christopher P E 1989a Spectral power determinations of compressibility and density variations in model media and calf liver using ultrasound *J. Acoust. Soc. Am.* **85** 423–31
Waag R C, Dalecki D and Smith W A 1989b Estimates of wave front distortion from measurements of scattering by model random media and calf liver *J. Acoust. Soc. Am.* **85** 406–15
Waag R C, Lee P P K, Persson H W, Schenk E A and Gramiak R 1982 Frequency-dependent angle scattering of ultrasound by liver *J. Acoust. Soc. Am.* **72** 343–52
Wear K A, Garra B S and Hall T J 1995 Measurements of ultrasonic backscatter coefficients in human liver and kidney *in vivo J. Acoust. Soc. Am.* **98** 1852–7
Whittle P 1954 On stationary processes in the plane *Biometrika* **41** 434–49
Whittle P 1962 Topographic correlation, power-law covariance functions, and diffusion *Biometrika* **49** 305–14
Whittle P 1963 Stochastic processes in several dimensions *Bull. Int. Stat. Inst.* **40** 974–94
Yao L X, Zagzebski J A and Madsen E L 1990 Backscatter coefficient measurements using a reference phantom to extract depth-dependent instrumentation factors *Ultrason. Imaging* **12** 58–70
Zagzebski J A, Lu Z F and Yao L X 1993 Quantitative ultrasound imaging: *in vivo* results in normal liver *Ultrason. Imaging* **15** 335–51